



HAL
open science

Analysis of suffusion in cohesionless soils with randomly distributed porosity and fines content

Jie Yang, Zhen-Yu Yin, Farid Laouafa, Pierre-Yves Hicher

► **To cite this version:**

Jie Yang, Zhen-Yu Yin, Farid Laouafa, Pierre-Yves Hicher. Analysis of suffusion in cohesionless soils with randomly distributed porosity and fines content. *Computers and Geotechnics*, 2019, 111, pp.157-171. 10.1016/j.compgeo.2019.03.011 . ineris-03319054

HAL Id: ineris-03319054

<https://ineris.hal.science/ineris-03319054>

Submitted on 11 Aug 2021

HAL is a multi-disciplinary open access archive for the deposit and dissemination of scientific research documents, whether they are published or not. The documents may come from teaching and research institutions in France or abroad, or from public or private research centers.

L'archive ouverte pluridisciplinaire **HAL**, est destinée au dépôt et à la diffusion de documents scientifiques de niveau recherche, publiés ou non, émanant des établissements d'enseignement et de recherche français ou étrangers, des laboratoires publics ou privés.

Analysis of suffusion in cohesionless soils with randomly distributed porosity and fines content

Jie YANG^{1,2}, Zhen-Yu YIN^{2,3}, Farid LAOUAFA^{1,*}, Pierre-Yves HICHER²

Affiliations:

¹ INERIS, Verneuil en Halatte, France

² Research Institute of Civil Engineering and Mechanics (GeM), UMR CNRS 6183, Ecole Centrale de Nantes, France

³ Key Laboratory of Geotechnical and Underground Engineering of Ministry of Education; Department of Geotechnical Engineering, College of Civil Engineering, Tongji University, Shanghai, China; Department of Civil and Environmental Engineering, The Hong Kong Polytechnic University, Hung Hom, Kowloon, Hong Kong, China

*Corresponding authors: Dr. Farid LAOUAFA, Tel.: +33 344556182; Email: farid.laouafa@ineris.fr

Abstract: Suffusion occurs when fines are plucked off by seepage forces and transported throughout the pores of the matrix constituted by coarser soil particles. Natural or human made soils are seldom homogeneous, which makes suffusion more complex. Suffusion is usually combined with the self-filtration of the fine particles and the transport of these fines may cause the soil structure to become looser. At the same time a clogging may occur which could reduce the permeability leading to an increase of excess pore pressure. The combination of these two phenomena will result in strength degradation. Currently, most suffusion analyses are performed without taking into account the soil's spatial variability. In this paper, a four-constituent continuum finite difference model for suffusion has been extended through the self-filtration process. A random field theory was at this point introduced into the finite difference code to investigate soil suffusion with a randomly distributed initial porosity and fines content. A probabilistic study using the Monte Carlo method was conducted to analyze the effect of the variance, the spatial correlation length, and the cross correlation of the randomly distributed initial porosity and fines content on the eroded mass and on the evolution of the hydraulic conductivity under 1D and 2D conditions. Based on all the simulations, it was possible to quantify the probability of particle blockage during erosion.

Keywords: granular media; probabilistic study; spatial variability; suffusion; filtration; soil heterogeneity

1 Introduction

One of the major causes of accidents in embankment dams and underground structures is internal erosion [1-6]. The known mechanisms are either leak erosion, backward erosion, soil contact erosion, or suffusion [7-9]. Among the above, suffusion is a complex phenomenon which appears as a combination of the detachment and transport of the finer particles by water flow, with filtration possibly occurring inside the voids between coarser particles, therefore changing the particle size distribution, the porosity, and the hydraulic conductivity of the soil. Consequently the soil's mechanical properties can become progressively degraded and, at a certain point, earthen structures may begin to suffer a risk of disorder such as ground subsidence, sinkholes, or landslides [1, 10-16]. Therefore, suffusion has been widely studied in the laboratory within the last decades [14, 17-27], particularly initiation and development of suffusion, the stress-strain behavior of eroded soil, as well as the effect of soil grading, the critical hydraulic gradient, critical pore water velocity in order to characterize the degree of susceptibility to suffusion.

Based on the findings in the afore-mentioned experiments, spatial and temporal progression of suffusion has also been studied and when the erosion tests were repeated, a significantly irregular deviation of hydraulic conductivity was noticed [24, 27-29]. This problem was attributed to the difference in homogeneity within the reconstituted soil specimens. However, another aspect, generally ignored, is to what extent the saturation stage may also influence the heterogeneity of the soil specimen before erosion.

Soil characteristics are highly variable in space [30-32]. Such spatial variations could be introduced by the processes of deposition or post-deposition including spatially varying diagenesis or formation and deformation of shear zones and discontinuities. In recent years, many studies have attempted to quantify the soil variability and to assess the resulting uncertainty for various applications. A number of studies have used stochastic approaches to investigate hydro-mechanical problems in geotechnical engineering. For instance, Freeze [33] performed 1D consolidation by introducing a cross correlation between the coefficient of volume compressibility and soil permeability; Badiou et al. [34] investigated 1D consolidation with the

thin layer method combined with Monte Carlo simulations; Huang et al. [35] performed systematic 1D and 2D random consolidation analyses over a range of parametric variations using the random field theory. Related works on foundation and slope problems using stochastic approaches can also be found [36-39].

However, the problem of suffusion has not yet been studied in a systematic probabilistic approach under the framework of the porous continuous medium theory. The aim of this study is to fill this gap by covering the following points: (1) to propose a four-constituent based finite difference model to describe the detachment of finer particles and the clogging of initial voids; (2) to implement within the model the random field theory for a Monte Carlo analysis under one-dimensional (1D) and two-dimensional (2D) conditions; (3) to analyze the influence of the soil heterogeneity on suffusion and to perform a systematic probabilistic study of suffusion. Both the initial porosity and fines content have been considered as random variables, for which the spatial correlation has been taken into account through the random field theory. The influence of the soil's spatial variability on clogging during suffusion can then be discussed.

2 Random finite difference analysis

2.1 Four-constituent suffusion governing equations

According to Schaufler et al. [40], it is possible to consider the saturated porous medium as a material system composed of 4 constituents: the solid skeleton, the erodible fines, the fluidized particles and the pure fluid. The fines can behave either as a fluid-like (described as fluidized particles) or as a solid-like (described as erodible fines) material. Thus, a liquid-solid phase transition process has been accounted for by the introduction of a mass production term in the corresponding mass balances for the 4 constituents. At a material point level, the mass balance for the i constituent is given, neglecting the hydro-mechanical dispersion tensor:

$$\frac{\partial(\rho^i)}{\partial t} + \text{div}(\rho^i \mathbf{v}^i) = \rho^{ex,i} \dots\dots\dots(1)$$

where ρ^i , $\rho^{ex,i}$ and \mathbf{v}^i denote, respectively, the partial density, the mass exchange term and the velocity of the corresponding constituent.

Considering the solid phase (solid skeleton and erodible fines), the mass balance for this species in the porous medium is

$$-\frac{\partial \phi}{\partial t} + \text{div}(\mathbf{v}_s) - \text{div}(\phi \mathbf{v}_s) = \hat{n} \dots\dots\dots (2)$$

The density of solid particles ρ_s is omitted at the two ends of the equation. Similarly, the mass balance equations for the erodible fines and the fluidized particles are:

$$\frac{\partial (f_c)}{\partial t} - \frac{\partial (f_c \phi)}{\partial t} + \text{div}(f_c \mathbf{v}_s) - \text{div}(f_c \phi \mathbf{v}_s) = \hat{n} \dots\dots\dots (3)$$

$$\frac{\partial (c\phi)}{\partial t} + \text{div}(c\mathbf{q}_w) + \frac{\partial (c\phi \mathbf{v}_s)}{\partial t} = -\hat{n} \dots\dots\dots (4)$$

$\phi(\underline{x}, t)$, $f_c(\underline{x}, t)$ and $c(\underline{x}, t)$ denote the bulk porosity, the fraction of the erodible fines in the solid skeleton and the concentration of the fluidized particles at the current spatial position \underline{x} at current time t ; \mathbf{v}_s is the velocity of the soil skeleton matrix; \mathbf{q}_w is the flow rate; \hat{n} is the source term describing the exchange between the erodible fines and the fluidized particles. For the sake of clarity, the time t and the spatial position \underline{x} variables have been omitted in our equations.

Finally, the mass balance of the mixture, i.e. the continuity equation, is

$$\text{div}(\mathbf{q}_w) + \text{div}(\mathbf{v}_s) = 0 \dots\dots\dots (5)$$

In this study, the flow in the porous medium is governed by Darcy's law which states that the flow rate is driven by the gradient of the pore fluid pressure p_w :

$$\mathbf{q}_w = -\frac{k(f_c, \phi)}{\eta_k \bar{\rho}(c)} \mathbf{grad}(p_w) \dots\dots\dots (6)$$

where $k(f_c, \phi)$ denotes the intrinsic permeability of the medium, η_k is the kinematic viscosity of the fluid, and $\bar{\rho}(c)$ is the density of the mixture defined as $\bar{\rho} = c\rho_s + (1-c)\rho_f$, with ρ_s the density of the solid and ρ_f the density of the fluid. For a material that is a mixture of coarse and

fine grains, the intrinsic permeability k of the porous medium depends on the current porosity ϕ and its fines content fraction f_c as [41]:

$$k = k_0 [1 - f_c (1 - \phi)]^{3m} \dots\dots\dots (7)$$

where m is the so-called ‘‘cementation exponent’’ which varies with the pore geometry.

2.2 Erosion law

The variable \hat{n} in Eqs. (2)-(4) is the volume of mass exchange, which corresponds to the rate of the eroded mass volume (\hat{n}_e) and the filtrated mass volume (\hat{n}_f) at any point in time:

$$\hat{n} = \hat{n}_e + \hat{n}_f \dots\dots\dots (8)$$

A model for the rate of the eroded mass is given by the following relation [42]:

$$\hat{n}_e = -\lambda_e (1 - \phi) (f_c - f_{c\infty}) |\mathbf{q}_w| \dots\dots\dots (9)$$

where $f_{c\infty}$ is the ultimate fines content fraction after a long seepage period, λ_e is a material parameter. $f_{c\infty}$ is assumed to decrease with the increase of the hydraulic gradient [43] as

$$f_{c\infty} = f_{c0} [(1 - \alpha_1) \exp(-|\mathbf{q}_w| \times 10^{\alpha_2}) + \alpha_1] \dots\dots\dots (10)$$

where f_{c0} is the initial fines content fraction, α_1 and α_2 are the material parameters. The term $(f_c - f_{c\infty})$ in Eq.(9) corresponds to the residual fines content fraction. The erosion rate depends not only on the total discharge of liquid \mathbf{q}_w but also on the residual fines content fraction.

However, with an increasing concentration of transported fine particles, the probability of the filtration phenomenon existing in the system of pore canals will also increase. The following model for the rate of the filtrated mass is suggested:

$$\hat{n}_f = \lambda_f \frac{\phi - \phi_{\min}}{\phi^\beta} c |\mathbf{q}_w| \dots\dots\dots (11)$$

where λ_f and β are the material parameters, ϕ_{\min} is the minimum porosity of the soil mixture. The probability of filtration increases with an increasing discharge of the fluidized particles ($c|\mathbf{q}_w|$). Moreover, the filtration process is expected to be more intense in intact regions which are characterized by smaller pore canals, *i.e.*, smaller porosity. β is related to the heterogeneity of the soil mixture.

2.3 Numerical modeling

The four-constituent erosion kinetic equations (2)-(5), coupled with the erosion-filtration constitutive law equations (8)-(11), make up an unsteady, coupled non-linear system of partial differential equations. The primary unknowns are the pore pressure p_w , the porosity ϕ , the fraction of fine content f_c , and the transport concentration c . This system of partially differential equations has been solved through an explicit finite difference procedure under a one-dimensional (1D) and a two-dimensional (2D) condition for a hydraulic-gradient controlled downward erosion tests on gap-graded sand and gravel mixtures performed by Zhong [44], shown in Figure 1. The oedo-permeameter consisted of a 285 mm inner diameter rigid wall cylinder cell, a pressurized water supply system and a water/soil collecting system. A stainless steel mesh screen was placed on the specimen support. The cell wall was equipped with twelve pressure ports (two arrays of six pressure ports, with a vertical spacing of 100 mm, face to face on opposite cell sides). The specimen of 430 mm in height was placed in the oedo-permeameter. A downward interstitial flow was forced through the specimen to investigate the susceptibility to suffusion after the saturation of the soil specimen.

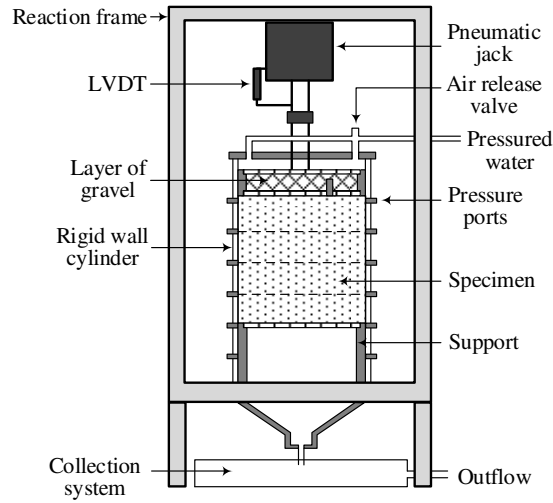


Figure 1. Schema of analyzed internal erosion test

Because of the non-linear nature of the analysis, computing the Monte Carlo simulations is labor and time intensive. In this study, the system of partially differential equations was first solved in 1D condition in order to obtain the main influences of the randomly distributed initial porosity and fines content and then, complemented by a set of 2D simulations, to evaluate the effects of dimensionality.

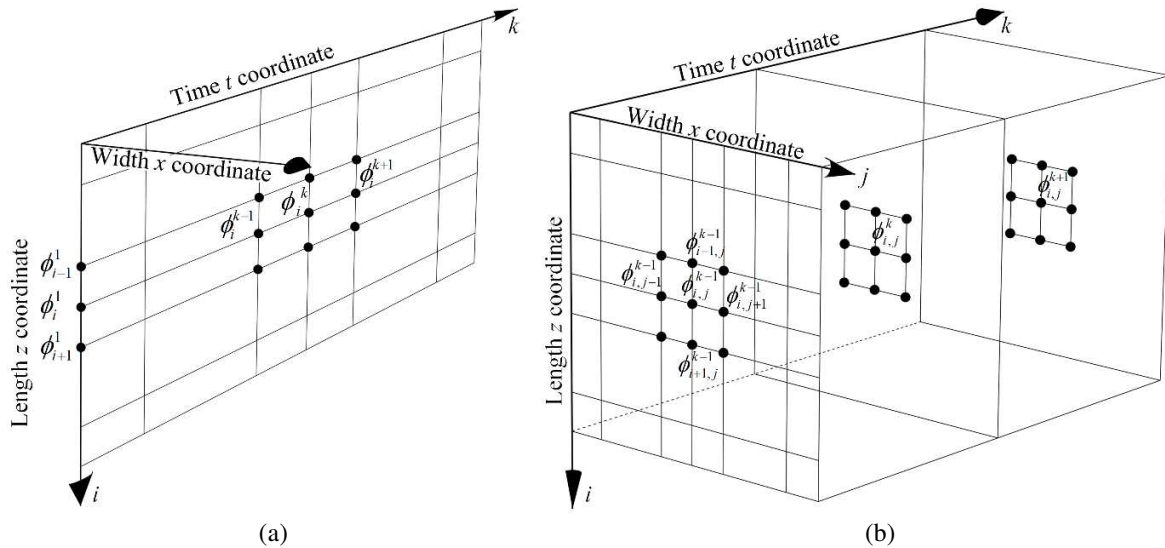


Figure 2. Finite difference grid of the primary unknowns (p_w , ϕ , f_c and c) in space-time of analyzed 1D and 2D internal erosion tests

With the terminology shown in Figure 2a in 1D condition, Eqs. (2), (4) and (5) become

$$\frac{\phi_i^{k+1} - \phi_i^k}{\Delta t} + [A_\phi]_i^k \frac{\phi_i^{k+1} - \phi_{i-1}^{k+1}}{\Delta z} + [B_\phi]_i^k \phi_i^{k+1} + [C_\phi]_i^k = 0 \quad \dots\dots\dots(12)$$

$$\frac{c_i^{k+1} - c_i^k}{\Delta t} + [A_c]_i^k \frac{c_i^{k+1} - c_{i-1}^{k+1}}{\Delta z} + [B_c]_i^k c_i^{k+1} + [C_c]_i^k = 0 \quad \dots\dots\dots(13)$$

$$\frac{p_{wi}^{k+1} - p_{wi}^k}{\Delta t} - \frac{[A_{p_w}]_{i+1/2}^k (p_{wi+1}^{k+1} - p_{wi}^{k+1}) + [A_{p_w}]_{i-1/2}^k (p_{wi}^{k+1} - p_{wi-1}^{k+1})}{(\Delta z)^2} = 0 \quad \dots\dots\dots(14)$$

where the subscripts $i(1, \dots, N_1)$ represent the variation in length, described by the z coordinate, and the subscripts $k(1, \dots, M)$ represent the variation in the time t coordinate. Similarly, this system of partially differential equations can be solved in 2D condition by:

$$\frac{\phi_{i,j}^{k+1} - \phi_{i,j}^k}{\Delta t} + [A_\phi]_i^k \frac{\phi_{i,j}^{k+1} - \phi_{i-1,j}^{k+1}}{\Delta z} + [A_\phi]_j^k \frac{\phi_{i,j}^{k+1} - \phi_{i,j-1}^{k+1}}{\Delta x} + [B_\phi]_{i,j}^k \phi_{i,j}^{k+1} + [C_\phi]_{i,j}^k = 0 \quad \dots\dots\dots(15)$$

$$\frac{c_{i,j}^{k+1} - c_{i,j}^k}{\Delta t} + [A_c]_i^k \frac{c_{i,j}^{k+1} - c_{i-1,j}^{k+1}}{\Delta z} + [A_c]_j^k \frac{c_{i,j}^{k+1} - c_{i,j-1}^{k+1}}{\Delta x} + [B_c]_{i,j}^k c_{i,j}^{k+1} + [C_c]_{i,j}^k = 0 \quad \dots\dots\dots(16)$$

$$\frac{p_{wi,j}^{k+1} - p_{wi,j}^k}{\Delta t} - \frac{[A_{p_w}]_{i+1/2}^k (p_{wi+1,j}^{k+1} - p_{wi,j}^{k+1}) + [A_{p_w}]_{i-1/2}^k (p_{wi,j}^{k+1} - p_{wi-1,j}^{k+1})}{(\Delta z)^2} - \frac{[A_{p_w}]_{j+1/2}^k (p_{wi,j+1}^{k+1} - p_{wi,j}^{k+1}) + [A_{p_w}]_{j-1/2}^k (p_{wi,j}^{k+1} - p_{wi,j-1}^{k+1})}{(\Delta x)^2} = 0 \quad \dots\dots\dots(17)$$

where the subscripts $j(1, \dots, N_2)$ represent the variation in width, described by the x coordinate. A , B and C are equation coefficients given in Appendix A.

f_c can be determined explicitly by the mass balance of the solid skeleton, leading to:

$$f_c = 1 - \frac{(1 + \varepsilon_v)(1 - \phi_0)(1 - f_{c0})}{1 - \phi} \quad \dots\dots\dots(18)$$

where ϕ_0 and f_{c0} denote the initial values of ϕ and f_c , respectively; ε_v denotes the volumetric strain calculated under the small strain assumption using an elastic model. This study focuses on the erosion-clogging process. The elastic model, therefore, has been used to calculate the

displacement field according to the sole pore pressure evolution. The strength degradation induced by the evolution of the porosity and the fines content may be discussed in future studies.

Eqs. (12)-(18) can then be coded and solved with the MATLAB software [45] with the given boundary conditions and initial values for p_w , ϕ , c :

$$(p_w)_{i=1,j}^k = p_0, (p_w)_{i=N_1,j}^k = p_L, c_{i=1,j}^k = c_0, c_{i=N_1,j}^k = c_{i=N_1-1,j}^k \dots\dots\dots(19)$$

$$(p_w)_{i,j}^1 = 0, c_{i,j}^1 = 0, \phi_{i,j}^1 = \phi_0(\underline{x}), (f_c)_{i,j}^1 = f_{c_0}(\underline{x}) \dots\dots\dots(20)$$

2.4 Random field modeling of initial porosity and fines content

In this study, the initial porosity ϕ_0 and the initial fines content fraction f_{c_0} within the soil mass are spatially varied. The initial fines content fraction f_{c_0} is assumed to be lognormally distributed with the mean value $\mu_{f_{c_0}}$, standard variation $\sigma_{f_{c_0}}$ and spatial correlation length $\theta_{\ln f_{c_0}}$. The lognormal distribution is one of many possible choices, which will guarantee non-negative soil properties. The lognormal distribution of f_{c_0} means that $\ln f_{c_0}$ is normally distributed and the standard variation $\sigma_{f_{c_0}}$ and mean $\mu_{f_{c_0}}$ of the normal distribution of $\ln f_{c_0}$ are given by:

$$\sigma_{\ln f_{c_0}} = \sqrt{\ln \left[1 + \left(\frac{\sigma_{f_{c_0}}}{\mu_{f_{c_0}}} \right)^2 \right]} \dots\dots\dots(21)$$

$$\mu_{\ln f_{c_0}} = \ln \mu_{f_{c_0}} - \frac{1}{2} \sigma_{\ln f_{c_0}}^2 \dots\dots\dots(22)$$

In this study, the random fields were generated with the local average subdivision (LAS) method [46]. Each discrete local average given by a realization becomes the average property within each discrete element. The lognormal random field $f_{c_0}(\underline{x})$ has been obtained by first simulating a normally distributed random field $G_{\ln f_{c_0}}(\underline{x})$, having zero mean, unit variance and an autocorrelation function $\rho_{\ln f_{c_0}}(\underline{x})$. An anisotropic exponential autocorrelation function has been adopted, which is expressed in 2D condition as:

$$\rho_{\ln f_{c_0}}(x, z) = \exp\left(\frac{-2|x|}{\theta_{\ln f_{c_0}, x}}\right) \exp\left(\frac{-2|z|}{\theta_{\ln f_{c_0}, z}}\right) \dots\dots\dots (23)$$

where $\theta_{\ln f_{c_0}, x}$ and $\theta_{\ln f_{c_0}, z}$ denote the horizontal and vertical correlation length of f_{c_0} , respectively; $|x|$ and $|z|$ denote the absolute coordinate differences of any two points of concern, in the horizontal and the vertical direction, respectively. After establishing the normally distributed random field, the required lognormally distributed random field is subsequently obtained as:

$$f_{c_0}(x) = \exp\left[\mu_{\ln f_{c_0}} + \sigma_{\ln f_{c_0}} G_{\ln f_{c_0}}(x)\right] \dots\dots\dots (24)$$

The initial porosity ϕ_0 is assumed to be higher than $\phi_{\min} > 0$. A beta distribution is often used for bounded random variables. Unfortunately, a beta distributed random field has a very complex joint distribution, and the simulation is difficult to perform. To simplify the procedure, we selected a shifted lognormal distribution, *i.e.* $\phi_n = (\phi_0 - \phi_{\min})$ is assumed to follow a lognormal distribution. The normally distributed random field $G_{\ln \phi_0}(x)$ has zero mean and unit variance as $G_{\ln f_{c_0}}(x)$. Conceivably, $\theta_{\ln \phi_0}$ is taken to be equal to $\theta_{\ln f_{c_0}}$, since it seems reasonable to assume that, if the spatial correlation structure is caused by changes in the constitutive nature of the soil over space, both ϕ_0 and f_{c_0} would have similar correlation lengths. Both lengths will be referred to simply as $\theta(\theta_x, \theta_z)$. A dimensionless correlation length is defined as

$$\Theta(\Theta_x, \Theta_y) = \frac{\theta(\theta_x, \theta_y)}{L}, \dots\dots\dots (25)$$

where L denotes the height of the specimen.

Since the cross correlation between ϕ_0 and f_{c_0} is unclear, the cross correlation extremes ρ have been investigated from -1 to 1 in order to determine if its chosen value is significant. The cross correlation between ϕ_0 and f_{c_0} has been implemented via the covariance matrix decomposition proposed by Fenton [47].

3 Deterministic simulation

In the internal erosion test performed by Zhong [44], the soil specimen was supposed to be initially homogeneous. However, the initial pore pressure along the specimen after the saturation stage, shown in Figure 3, confirmed the initial heterogeneity along the specimen. This initial heterogeneity may have been caused, on one hand, by the compaction of the reconstituted soil specimen and, on the other hand, by the impact of the saturation stage. The initial profiles of porosity ϕ and fines content f_c were, therefore, calibrated by fitting the initial pore pressure along the specimen, summarized in Table 1, named “Case 0”. The thickness of the i th layer is h_i .

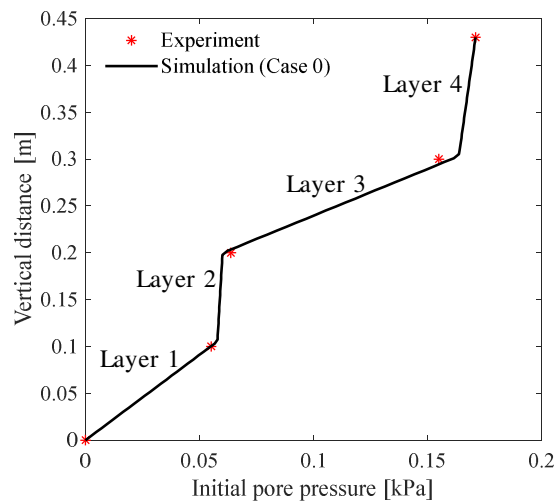


Figure 3. The initial pore pressure at the beginning of the erosion stage

Table 1. Initial profiles of porosity and fine content

Case 0				Case 1				Case 2			
i layer	h_i [mm]	ϕ_0	f_{c0}	i layer	h_i [mm]	ϕ_0	f_{c0}	i layer	h_i [mm]	ϕ_0	f_{c0}
1	100	0.30	0.28	1	224	0.29	0.30	1	100	0.31	0.27
2	100	0.38	0.19	2	206	0.38	0.19	2	100	0.35	0.24
3	100	0.29	0.30					3	100	0.31	0.27
4	130	0.36	0.22					4	130	0.36	0.22

After the soil became saturated, the fluid was forced to flow downwards through the specimen during the erosion test. A multi-stage hydraulic gradient condition consisted of increasing by

steps the hydraulic gradient from 0.04 to 0.5. Each stage of the hydraulic gradient was kept constant for about 30 min. The physical properties of the soil mixture are summarized in Table 2. The model parameters were calibrated by fitting the time evolution of the hydraulic conductivity and the cumulative loss of the dry mass of the soil mixture, using an optimization technique [48, 49]. All the values determined for the model parameters, summarized in Table 3, were used in the following analyses.

Table 2. Physical properties of the soil mixtures according to [44]

Density of fluid	ρ_f	1.0 g/cm ³
Density of solids	ρ_s	2.65 g/cm ³
Kinematic viscosity of fluid	η_k	5.0×10 ⁻⁶ m ² s ⁻¹
Minimum porosity	ϕ_{\min}	0.2
Initial permeability	k	3.6×10 ⁻³ m/s

Table 3. Values of model parameters for tested soil mixtures

Erosion parameters			Filtration parameters		Permeability parameters
λ_e	α_1	α_2	λ_f	β	m
14.0	0.88	4.0	0.6	7.2	10.7

In Figure 4, the experimental and numerical results of the erosion test are compared. The hydraulic conductivity of the specimen is shown in Figure 4a. It can be seen that the numerical model was able to reproduce the two phases of the erosion up to a stable stage. The decrease of the hydraulic conductivity in the first phase was accompanied by a clogging of the pores. A clogging, which at first restricted the water flow, could then be blown away, leading to a significant increase of the hydraulic conductivity. Therefore, the second phase of the hydraulic conductivity evolution could be characterized by its rapid increase. The hydraulic conductivity reached at last a constant value and tended to stabilize when the hydraulic drag force could no longer transport any more fine particles through the soil skeleton. Figure 4b plots the time evolution of the cumulative eroded masses. The two-phase process of the erosion can be clearly identified. Experimental and numerical values of the eroded mass agree well with each other.

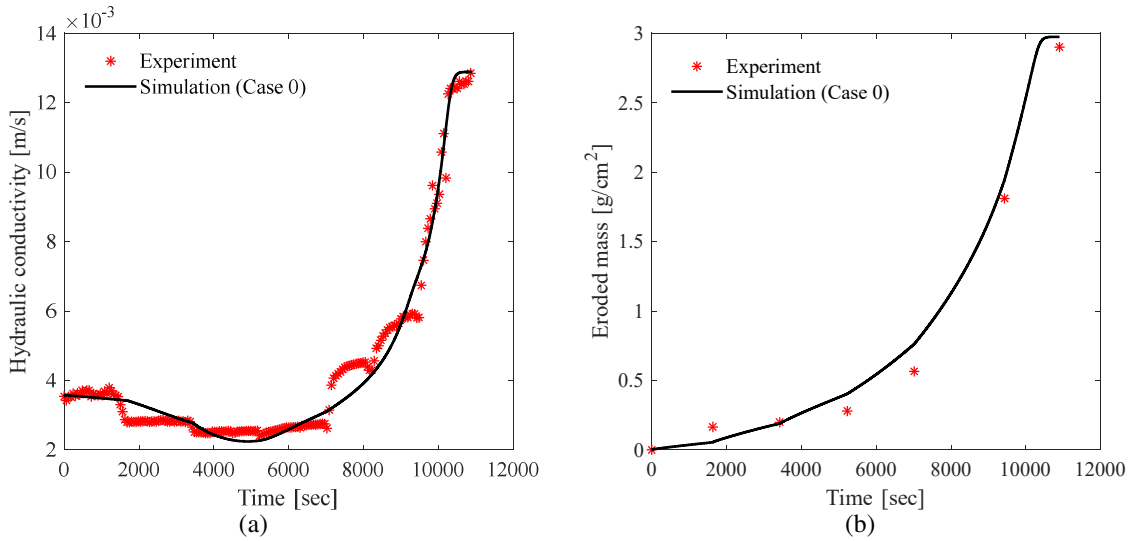


Figure 4. Comparison between laboratory test (symbols) and simulated data (continuous lines): (a) time evolution of hydraulic conductivity; (b) time evolution of cumulative eroded masses

The spatial profiles at different time steps of the porosity and the concentration of the fluidized fine particles are shown in Figure 5. Corresponding to the decrease of the hydraulic conductivity in the first phase shown in Figure 4a, the clogging of the pores was observed at the interface where the porosity dropped at $t = 2180$ s and 4360 s in Figure 5a. This indicates that the fluidized fine particles were filtrated at the interfaces. It is more clearly shown in Figure 5b by the drop of the transport concentration at the interfaces. As a consequence of the actual boundary conditions, a front of concentration (steep gradient of concentration) was observed passing through the domain from the inlet to the outlet. The clogging began to be unblocked when the front of concentration reached the clogging, accompanied by the increase of the hydraulic conductivity. The erosion-filtration process stopped when the ultimate fines content fraction f_{∞} was attained, determined by Eq. (10).

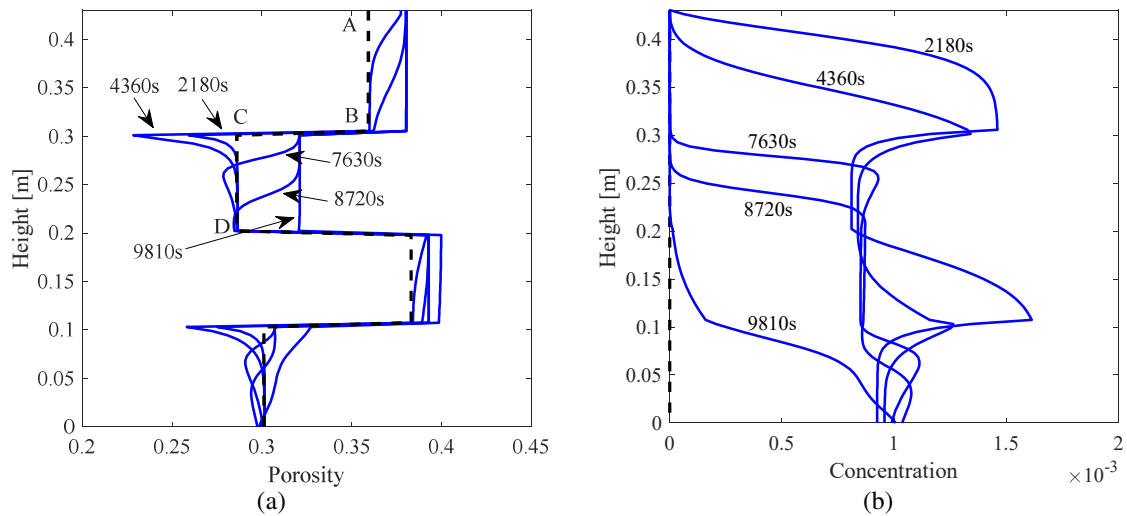


Figure 5. Spatial profiles of (a) porosity and (b) concentration of fluidized fine particles, respectively at various time steps (the dashed black lines indicate the initial profiles)

Note that the proposed model is well-suited for simulating a filter cake formation caused by clogging. A filter cake is a localized layer of highly reduced permeability. In a 1D domain, it is divided into two parts (Figure 6). Two different types of filter cakes might occur [40, 50, 51]. First, it is possible for an external filter cake to form at the interface where the constriction sizes of the pore channels are smaller than the average diameter of the fluidized fines. Hence, the fines are unable to penetrate significantly into the downstream part of the domain. Rather, the fines are deposited at the border between the layers. On the other hand, an internal filter cake is formed if the fines do penetrate into the second part of the domain. As more particles accumulate, a layer with reduced permeability will develop. In 2D condition, as the influx can bypass the local blockage, the permeability of the specimen will not decrease until a continuous clogged layer is formed. It has to be pointed out, however, that the proposed model can apply to cases of internal filter cakes only. To capture the occurrence of an external filter cake, it is necessary to consider a geometrical analysis of the constriction size distribution.

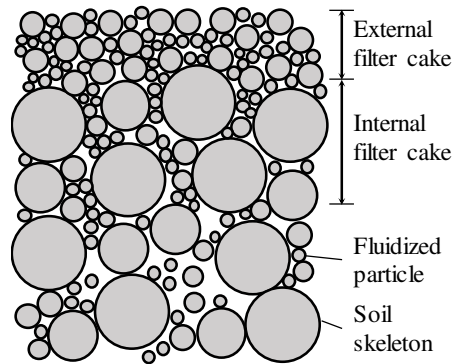


Figure 6. Schematic of filter cake (external and internal) in porous media

To analyze how the soil heterogeneity influences the suffusion, it was decided to simulate 3 additional presumed cases with different initial profiles of porosity and fines content. The mean ϕ_0 and f_{c0} for each case were kept at 0.33 and 0.25, respectively, while the variations of ϕ_0 and f_{c0} , and the thickness of the layers were varied according to Table 1. Compared to Case 0, Case 1 has the same variation of ϕ_0 and f_{c0} but only 2 layers; Case 2 has 4 layers, but a smaller variation. For Case 3, ϕ_0 and f_{c0} are uniformly distributed.

Figure 7 clearly demonstrates that assuming a homogeneous soil condition is insufficient in predicting the decrease of the hydraulic conductivity. By comparing the rate of eroded mass and the minimum value of the hydraulic conductivity of the specimen during the test period, it could be seen that the more heterogeneous the specimen, the slower the eroded mass increased and the more severe the clogging became. In the following sections, the influence of the initial profiles of porosity ϕ_0 and fine content f_{c0} will be systematically discussed through an analysis of the sensitivity of the rate of eroded mass and the minimum hydraulic conductivity during the test period to the randomly generated ϕ_0 and f_{c0} .

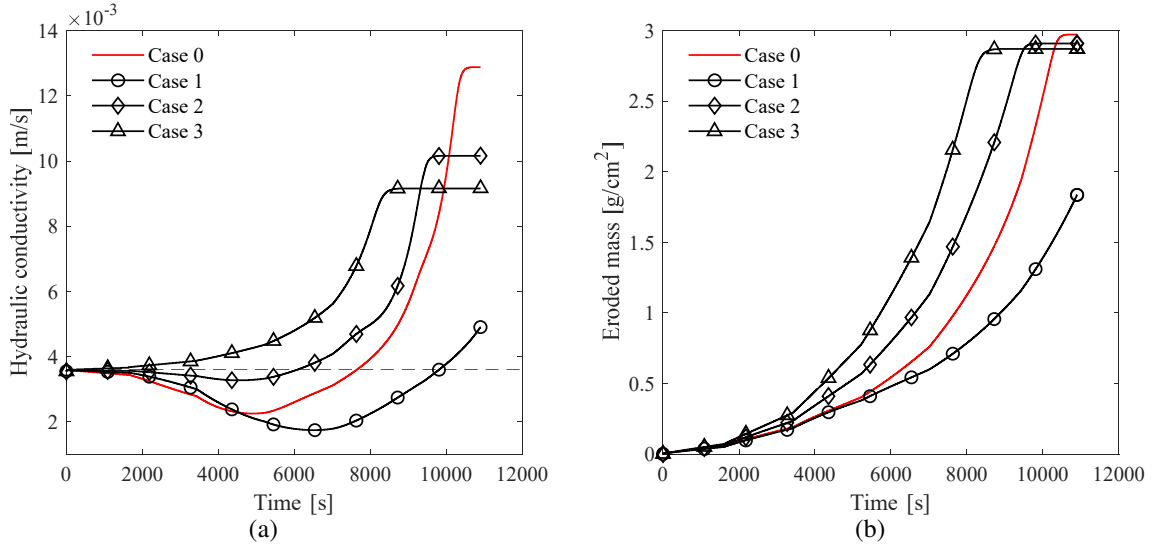


Figure 7. Time variation of (a) hydraulic conductivities and (b) cumulative eroded masses for the layered soils

4 Monte Carlo simulations in 1D condition

1D Monte Carlo simulations were firstly performed on the above configuration (with length $L=0.43\text{m}$) to investigate the sensitivity of the eroded mass and the hydraulic conductivity of the specimen to the randomly generated ϕ_0 and f_{c0} . The mean ϕ_0 and f_{c0} , referred to as μ_{ϕ_0} and $\mu_{f_{c0}}$, respectively, were kept at 0.33 and 0.25, while the coefficient of variation COV ($=\sigma/\mu$), the normalized spatial correlation length Θ ($=\theta/L$), for both ϕ_0 and f_{c0} , and the cross-correlation coefficient ρ were changed systematically, according to Table 4.

Table 4. Random field parameters used in the study

COV	0.05	0.1	0.15	0.2	
Θ	0.25	0.5	1.0	2.0	4.0
ρ	-1.0	0.0	1.0		

In fact, the coefficient of variance of ϕ_0 and f_{c0} may be different. The reason for using the same value of COV for both ϕ_0 and f_{c0} in this paper is only for the purpose of comparison. Not much data is available to indicate the level of correlation between ϕ_0 and f_c . Strong negative or positive correlation between the porosity and the fines content fraction for sand-silt mixtures has

been shown by Yin et al. [15] for different conditions. For the purpose of this paper's probabilistic study, the cross-correlation coefficient between ϕ_0 and f_c was set to -1.0, 0.0 and 1.0.

4.1 Determination of the number of MCS runs

When using the Monte Carlo simulations (MCS), the number of runs should be first determined to obtain converged results. For the sake of accuracy and run-time efficiency, the sensitivity of the results to the number of Monte Carlo simulations was examined. The “worst” cases with the highest $COV = 0.2$ and $\Theta = 0.25$ were chosen to investigate the effect of the number of simulations on the output quantities. Figure 8 shows the convergence of the ultimate eroded mass and the ultimate hydraulic conductivity of the specimen as the number of simulations increases. It can be seen that 2000 simulations were enough to provide reliable and reproducible estimates. Hence, for each parametric combination in the following studies, 2000 Monte Carlo simulations were performed.

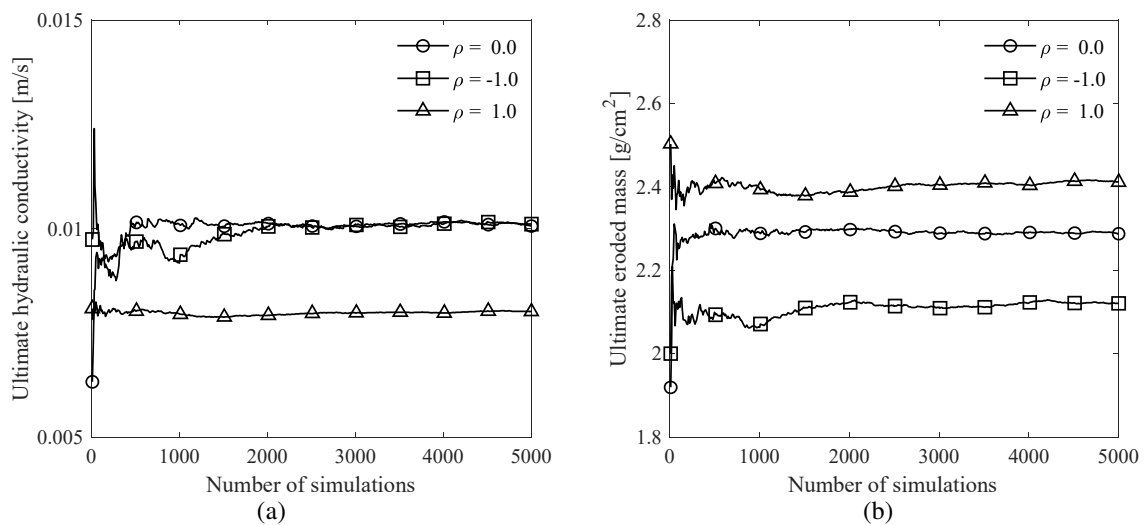


Figure 8. Influence of the number of Monte Carlo simulations on (a) ultimate eroded mass and (b) ultimate hydraulic conductivity ($COV = 0.2$ and $\Theta = 0.25$)

4.2 Simulation results

Figure 9 shows how the sample mean rate of eroded mass \dot{m} and minimum hydraulic conductivity during the test period k_{\min} , taken as the average over the 2000 realizations and

referred to as μ_{in} and $\mu_{k_{min}}$, respectively, vary with correlation length, soil variability, and cross-correlation between ϕ_0 and f_{c0} . In 1D analyses, an increase of soil variability generally decreased the mean rate of the eroded mass and the mean minimum hydraulic conductivity during the test period. These results illustrate that the higher the soil variability, the greater the number of transported fine particles are captured and re-deposited within the soil skeleton. This may be explained by the fact that a higher variability is accompanied by severer transitions between dense and loose layers in the specific domain, which facilitates the filtration process. The greatest reduction of μ_{in} and $\mu_{k_{min}}$ induced by the clogging are observed for negatively correlated ϕ_0 and f_{c0} ($\rho = -1$), the least reduction when ϕ_0 and f_{c0} are perfectly correlated ($\rho = 1$), and the independent case ($\rho = 0$) lies between these two extremes. The sample mean is more strongly affected by the soil variability and somewhat less so by the cross-correlation between ϕ_0 and f_{c0} .

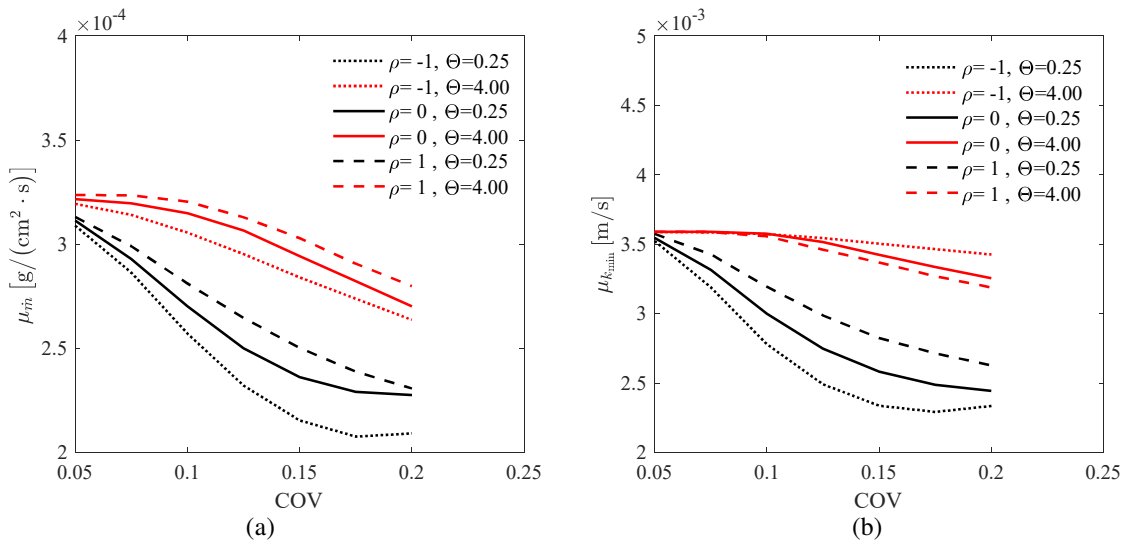


Figure 9. Sample mean of (a) rate of eroded mass μ_{in} , and (b) minimum hydraulic conductivity during the test period $\mu_{k_{min}}$

Figure 9 also shows that the dimensionless correlation length, Θ , has a significant influence. The variations of μ_{in} and $\mu_{k_{min}}$ with respect to Θ are more clearly seen in Figure 10. In a 1D analysis, an increase of Θ generally increased μ_{in} and $\mu_{k_{min}}$. A higher Θ makes the layered

system more uniform, thus leading to a smoother transition between the dense and loose layers. As a consequence, the filtration process is reduced and, in turn, the sample mean rate of eroded mass and minimum hydraulic conductivity during the test period will increase.

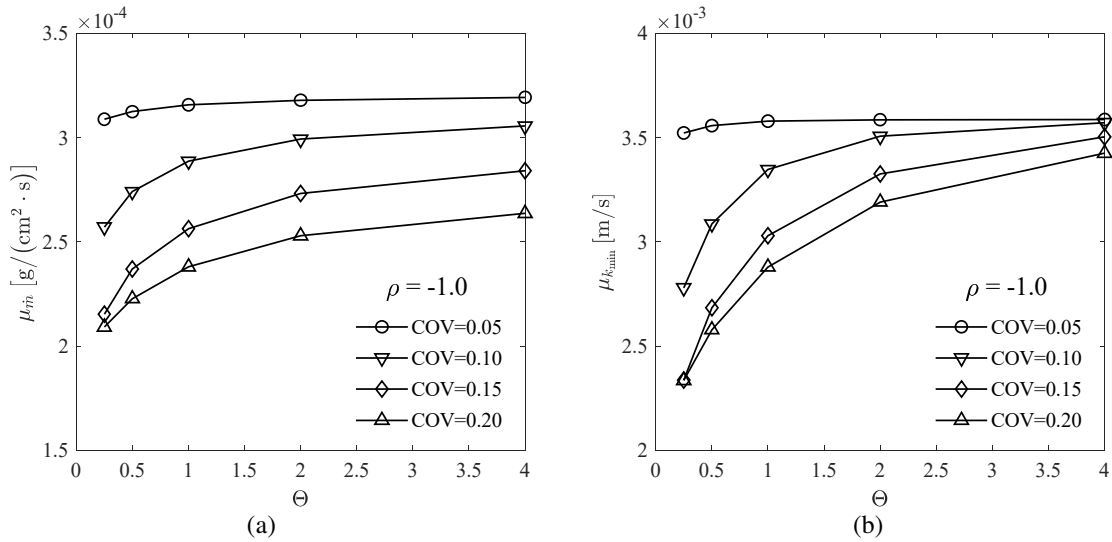


Figure 10. $\rho = -1.0$, comparison of: (a) the mean final cumulative eroded mass; (b) the mean minimum hydraulic conductivity during suffusion process

The usual simulation practice for suffusion is based on the sole mean values in homogeneous soil. The above results confirm that the erosion rate and the evolution of the hydraulic conductivity are different in heterogeneous soil with consideration to the soil variability and the spatial correlation length. What this implies from a design standpoint is that the susceptibility of soil to internal erosion may be different with that obtained in deterministic analysis in homogeneous soil.

4.3 Probabilistic interpretation

The plucking-off of the fine particles and the transport of these fines may cause the soil structure to become looser. At the same time clogging may occur which could reduce permeability and lead to an increase of excess pore pressure. The combination of these two phenomena will result in the strength degradation of the soil [16]. Figure 11 shows the time histories of the normalized hydraulic conductivity of the specimen with different input statistics. The probability of blockage during suffusion can be defined by counting the number of simulations in which the hydraulic

conductivity during the erosion simulation is smaller than its initial value, *i.e.*, counting the number of simulations in which $[k/k_{ini} < 1.0]$ and dividing it by the total number of simulations. Figure 12 compares the probability of blockage during the suffusion simulations with different coefficients of cross correlation, different lengths of correlation, and different coefficients of variation of ϕ_0 and f_{c0} .

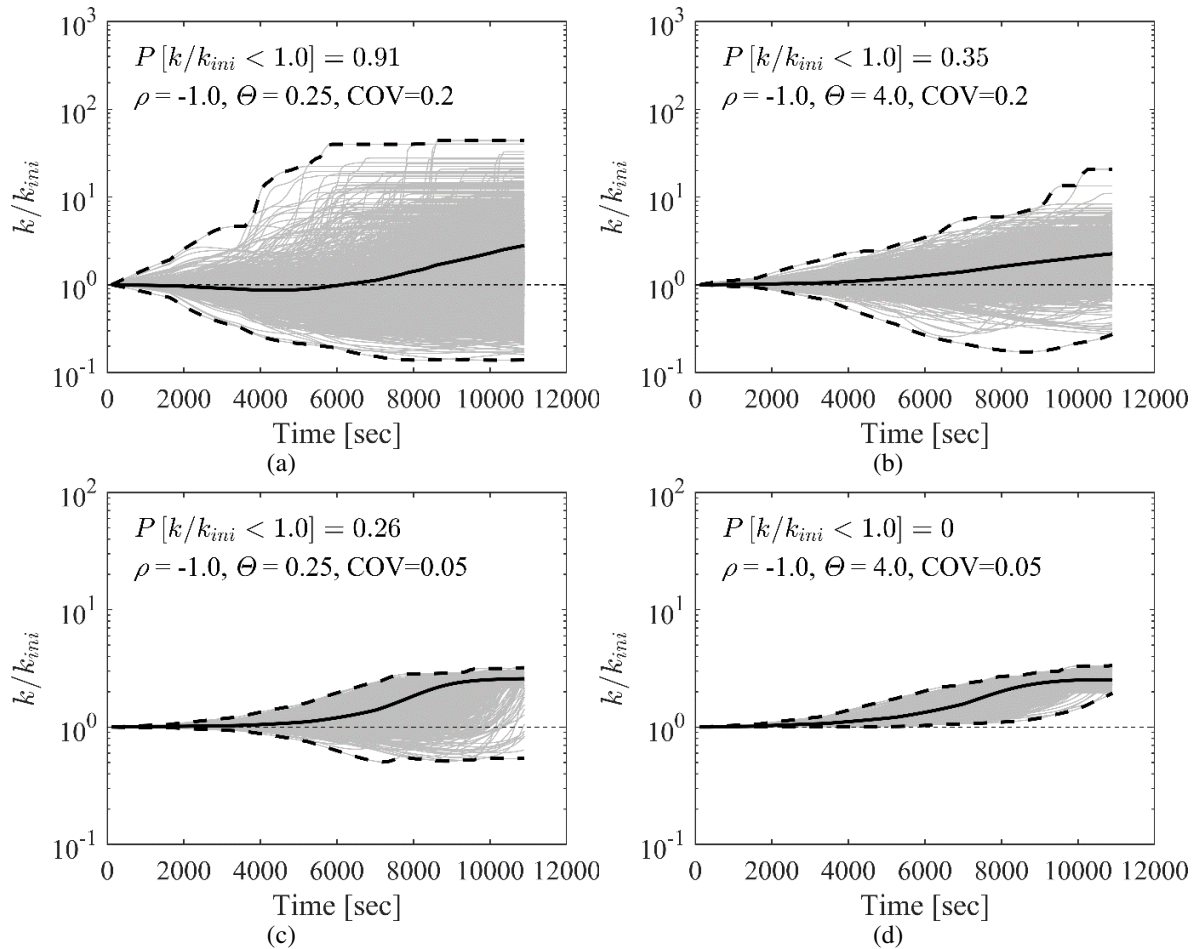


Figure 11. Time histories of normalized hydraulic conductivity of the specimen with different soil uncertainties, $\rho = -1.0$: (a) $\Theta = 0.25$, $\nu = 0.2$; (b) $\Theta = 4.0$, $\nu = 0.2$; (c) $\Theta = 0.25$, $\nu = 0.05$; (d) $\Theta = 4.0$, $\nu = 0.05$

The results indicate that an increase of the variability in ϕ_0 and f_{c0} values will generally increase the probability of blockage during suffusion. This can be explained by the fact that a greater variability will lead to more dramatic changes of soil porosity and permeability at the

interface of the different layers, which in turn facilitates the capture of the fine particles transported within the water flow. Moreover, the random fields of ϕ_0 and f_{c0} values with lower spatial correlation lengths make the layered system more uneven, therefore accelerating the formation of filter cakes at the interface. Moreover, negatively correlated ϕ_0 and f_{c0} are likelier to cause blockage.

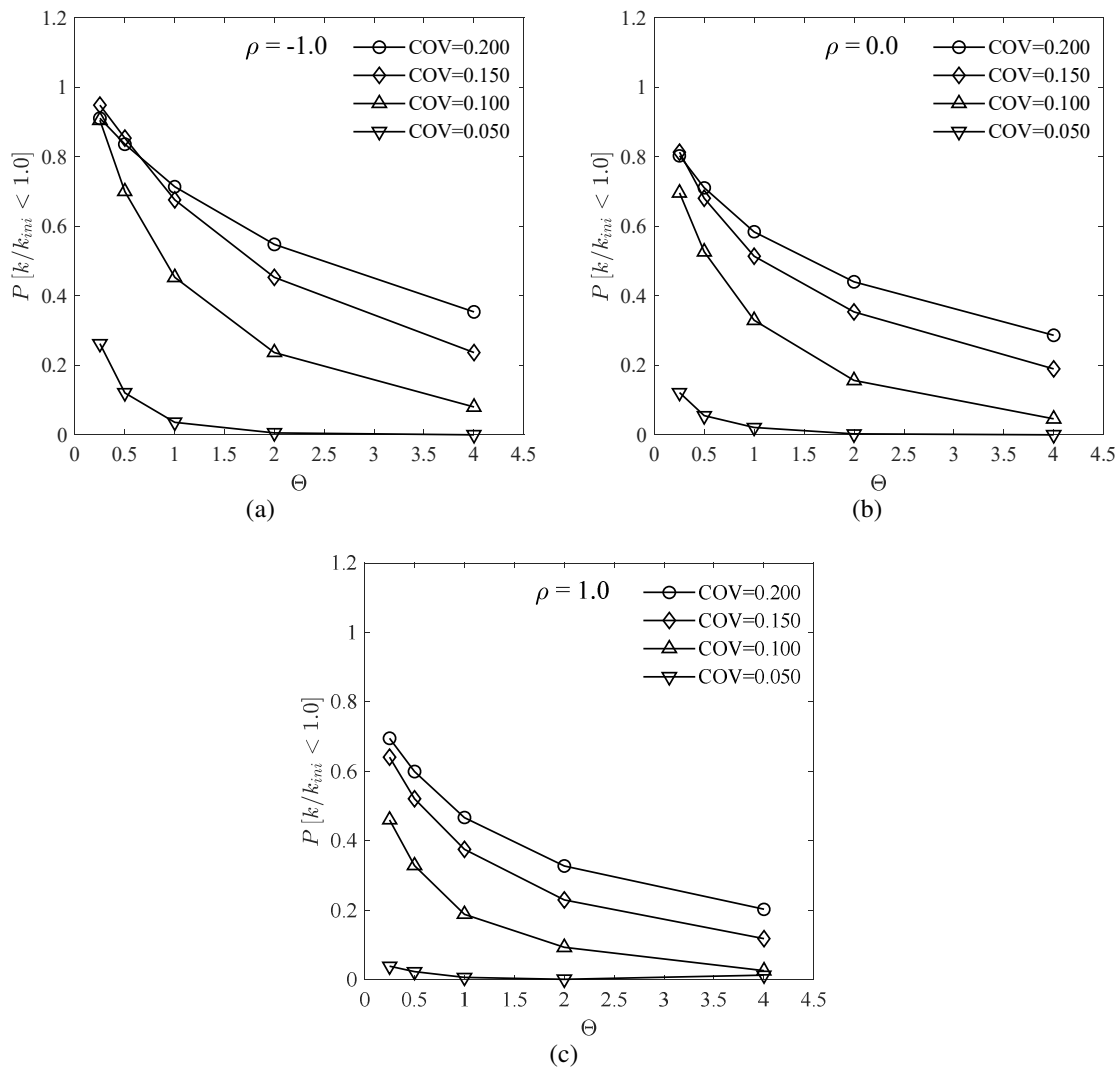


Figure 12. Comparison of probability of blockage during suffusion process: (a) $\rho = -1.0$; (b) $\rho = 0.0$; (c) $\rho = 1.0$

The susceptibility of soil to internal erosion when its spatial variability is considered may be different from that which is obtained by a deterministic analysis in a homogeneous soil. The probability of blockage increases significantly when the soil variability increases and when the spatial correlation length decreases, resulting in the increase of the risk of damage of linear earthen structures such as levees, dikes, etc., induced by the pore pressure increase.

5 Monte Carlo simulations in 2D condition

In 2D condition, the influx can bypass the local blockage, which leads to the decrease of the permeability at blockage. The part below investigates how the spatial correlation lengths of ϕ_0 and f_{c0} influence suffusion in both isotropic and layered anisotropic 2D random fields. 7 cases with different magnitudes of the spatial correlation length in isotropic fields and 5 cases with different horizontal and vertical correlation lengths in an anisotropic field are shown in Table 5. Because the horizontal correlation length is often larger than the vertical correlation length, the anisotropic ratio $r_{xy} = \Theta_x / \Theta_y$ is set > 1 with a constant $\Theta_y = 0.25$ in the following anisotropic cases.

Table 5. Spatial correlation length in 2D random fields

Case	Correlation length Θ_x	Correlation length Θ_y
ISO-1	0.05	0.05
ISO-2	0.1	0.1
ISO-3	0.25	0.25
ISO-4	0.5	0.5
ISO-5	1.0	1.0
ISO-6	2.0	2.0
ISO-7	4.0	4.0
ANI-1	0.5	0.25
ANI-2	1.0	0.25
ANI-3	2.0	0.25
ANI-4	4.0	0.25
ANI-5	250.0	0.25

Figure 13 shows six realizations of the generated random fields of initial porosity with different spatial correlation lengths. It appears evident that in isotropic random fields, when Θ decreases, any point at which the porosity is lower is surrounded by points where the porosity is higher. The

diffused loose area or dense area tends to be connected into blocks as the correlation length increases in both horizontal and vertical directions. In anisotropic random fields, the soil domain tends to be horizontally stratified, as the horizontal correlation length becomes increasingly larger than the vertical correlation length. It should be noted that the COV and the cross-correlation of ϕ_0 and f_{c0} are fixed at 0.1 and -1 for all the cases shown in Table 5.

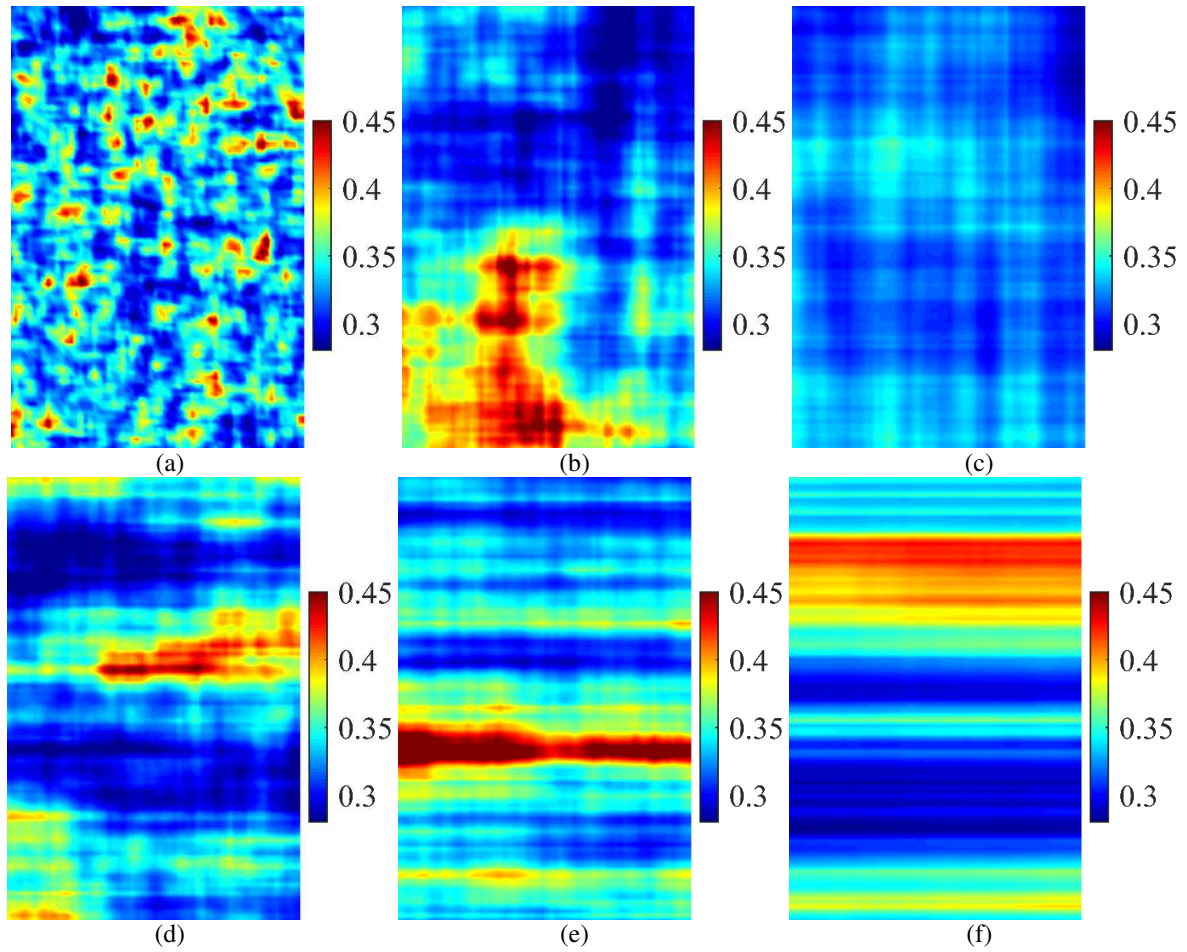


Figure 13. Generated random fields of initial porosity according to different spatial correlation length: (a) Case ISO-1: $\Theta_x = \Theta_y = 0.05$; (b) Case ISO-4: $\Theta_x = \Theta_y = 0.5$; (c) Case ISO-6: $\Theta_x = \Theta_y = 2.0$; (d) Case ANI-2: $\Theta_x = 1.0$, $\Theta_y = 0.25$; (e) Case ANI-4: $\Theta_x = 4.0$, $\Theta_y = 0.25$; (f) Case ANI-5: $\Theta_x = 250.0$, $\Theta_y = 0.25$

5.1 Single realization

A simulation example of a 2D suffusion in a non-homogeneous field for a single realization is shown in Figures 14 to 17. Figure 14 shows the randomly generated initial porosity and fines content for statistics inputs $\mu_{\phi_0} = 0.33$ and $\mu_{f_{c0}} = 0.25$, $\text{COV} = 0.1$, $\Theta_x = \Theta_y = 0.25$ and $\rho = -1$. In Figure 14a, the blue areas correspond to low porosity where the transported fine particles can be filtered more easily, and the red areas correspond to high porosity.

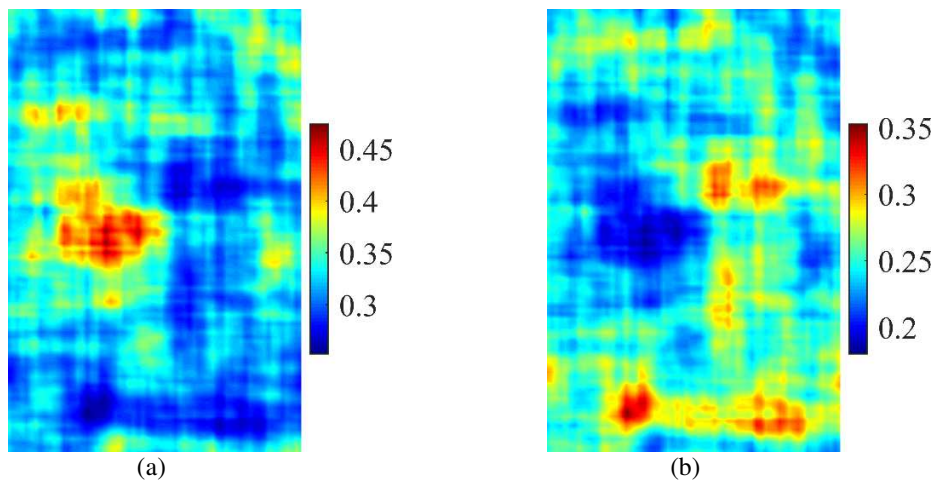


Figure 14. 2D stochastic simulation for a single realization (a) initial porosity; (b) initial fraction of fine content

The time evolution of the hydraulic conductivity of the specimen and the cumulative eroded masses are shown in Figure 15. Figures 16 and 17 illustrate the evolution of the fines content and the porosity with respect to its initial state at 5 different time steps corresponding to points A to E shown in Figure 15. The fine particles were firstly detached in the vicinity of the inlet, transported downwards and partially captured within the denser area. From the start to time step A, erosion and filtration proceeded simultaneously in a rather diffused manner. No area was continuously clogged; no preferential flow channel was formed, all of which contributed to the initial stable stage of hydraulic conductivity. From time step A, the diffused clogged areas began to unite. The clogged area can be seen more clearly in Figure 17. A clogged layer can be observed at the lower part of the specimen, which explains the decrease of the hydraulic conductivity. Furthermore, from Figure 16b and Figure 16c, it seems that the influx has bypassed the denser area at the top of the specimen. From time step C, the clogged area begins to be

unblocked. A preferential channel can be observed at the bottom left of the specimen in Figures 16d and 17d, which explains the significant increase of the hydraulic conductivity. The clogging, restricting at first the water flow, was then blown away. This stage is characterized by a rapid increase of hydraulic conductivity.

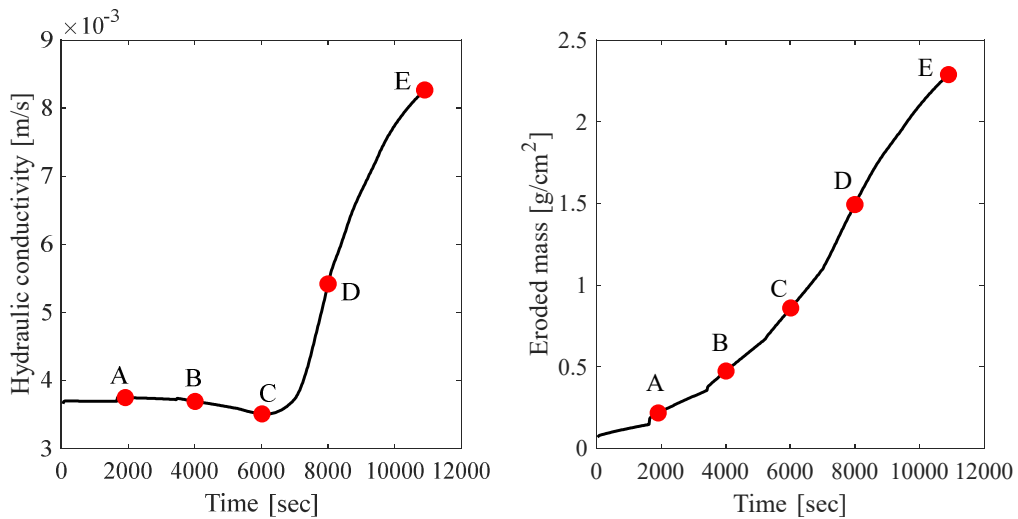
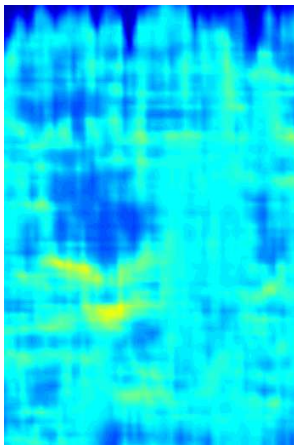
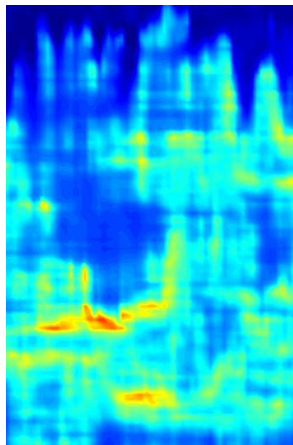


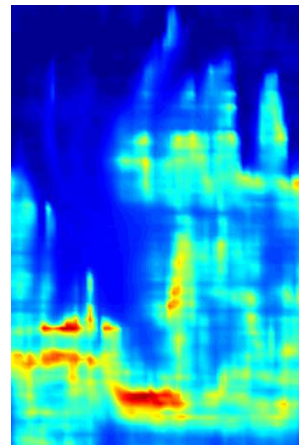
Figure 15. 2D stochastic simulation for a single realization (a) time evolution of hydraulic conductivity; (b) time evolution of cumulative eroded masses



(a) Time step A



(b) Time step B



(c) Time step C

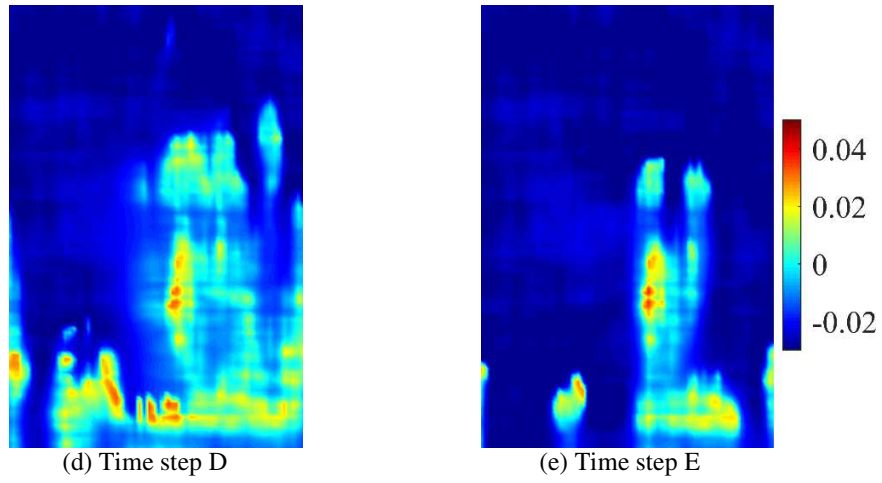


Figure 16. The evolution of fine content at different time steps with respect to its initial state for the single realization

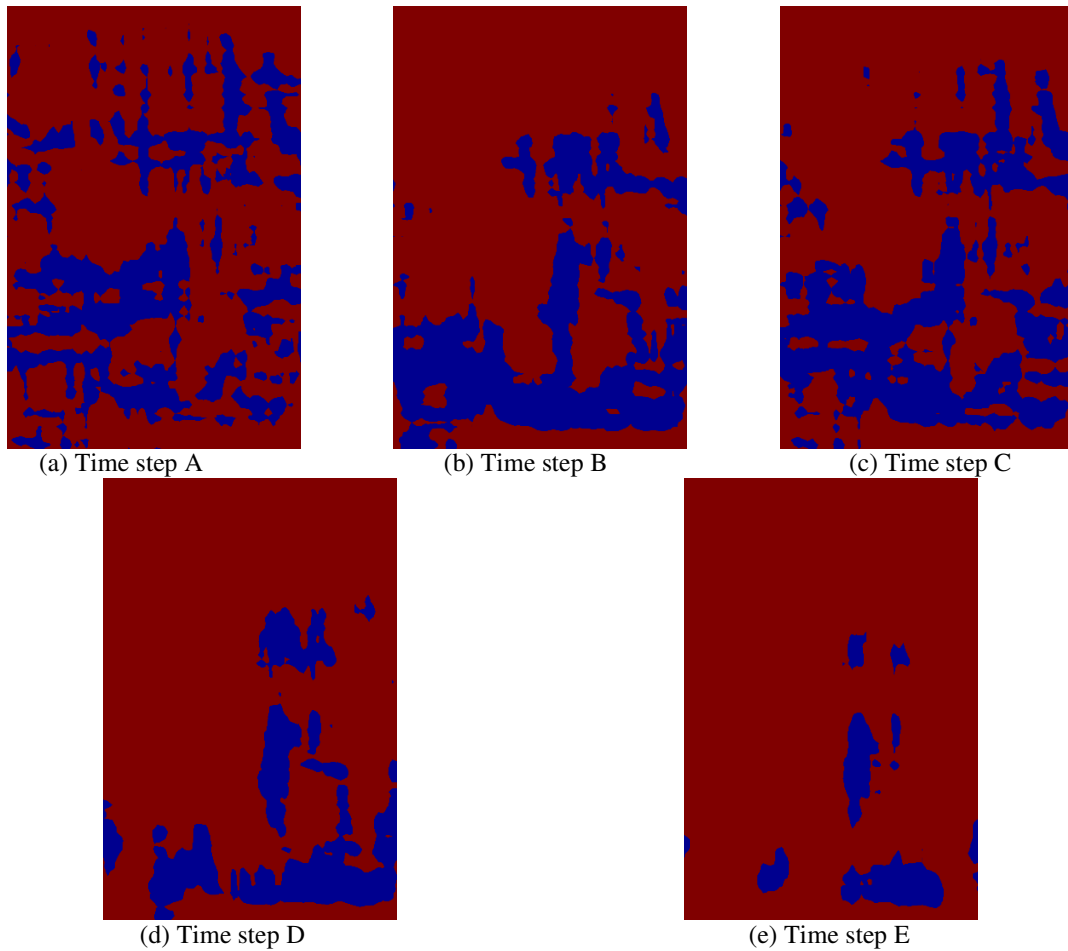


Figure 17. The evolution of porosity at different time steps with respect to its initial state for the single realization (the blue area indicates the clogged area, the red area indicates the eroded area)

5.2 Influence of spatial correlation in 2D random fields

The comparison between 1D and 2D isotropic analyses is shown in Figure 18. The mean rates of the eroded mass μ_m in 2D condition are generally smaller than that in 1D condition. Interestingly, the greatest reduction in μ_m in 2D condition occurs when the spatial correlation length θ is about half of the specimen length L , while in 1D condition, μ_m increases monotonically with θ . The same trend was found in the evolution of the probability of blockage, as shown in Figure 18c. The highest probability of blockage in 2D condition occurs when θ is between $0.3L$ and $0.5L$, while the probability of blockage in 1D condition keeps decreasing from 1 when θ is extremely small ($\theta=0.05L$ in this case). This can be explained by the fact that, as the correlation length drops down to zero, the random field becomes infinitely rough with all points in the field becoming independent of each other. Therefore, in 1D condition, more filter cakes will form at the interface of different layers, which leads to the decrease of $\mu_{k_{\min}}$ and $P[k/k_{ini} < 1.0] \rightarrow 1.0$ as $\theta \rightarrow 0$. However, in 2D condition, the locally denser areas are scattered throughout the whole region, as shown in Figure 13a, which hinders the formation of the continuous clogged layer, leading to $\mu_{k_{\min}} \rightarrow k_{ini}$ and $P[k/k_{ini} < 1.0] \rightarrow 0$ as $\theta \rightarrow 0$. When the correlation length increases to infinity, the random field becomes spatially constant, albeit still random, from realization to realization. In this case, fewer transported fine particles can be filtrated, which leads, on the one hand, to the increase of $\mu_{k_{\min}}$ and, on the other hand, to the decrease of $P[k/k_{ini} < 1.0]$.

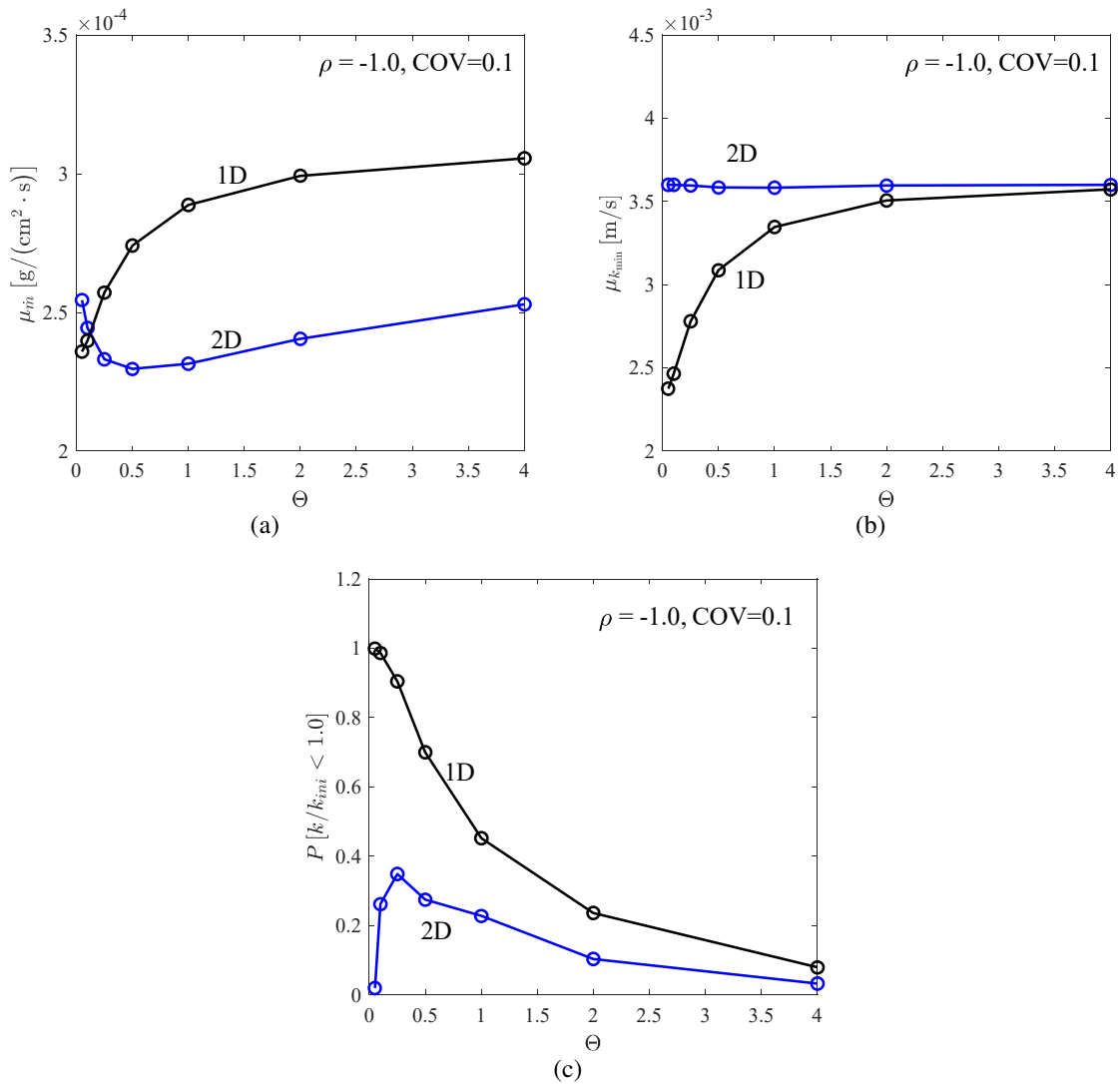


Figure 18. Comparison between 1D and 2D isotropic analyses (a) mean rate of eroded mass μ_m , (b) mean minimum hydraulic conductivity during the test period $\mu_{k_{\min}}$ and (c) probability of blockage

From Case ISO-3 and cases ANI-1 to ANI-5, the anisotropic ratio $r_{xy} = \Theta_x/\Theta_y$ increases from 1 to 1000, as Θ_x increases from 0.25 to 250 with a constant Θ_y at 0.25. Figure 19 shows the variation of the mean values of the eroded mass rate and the minimum hydraulic conductivity during the test period, as well as the probability of blockage when r_{xy} is increased. Obviously μ_m

and $P[k/k_{ini} < 1.0]$ are always lower and $\mu_{k_{min}}$ is always higher in 2D rather than in 1D. One can anticipate the three-dimensional (3D) values of μ_m and $P[k/k_{ini} < 1.0]$ to be also lower.

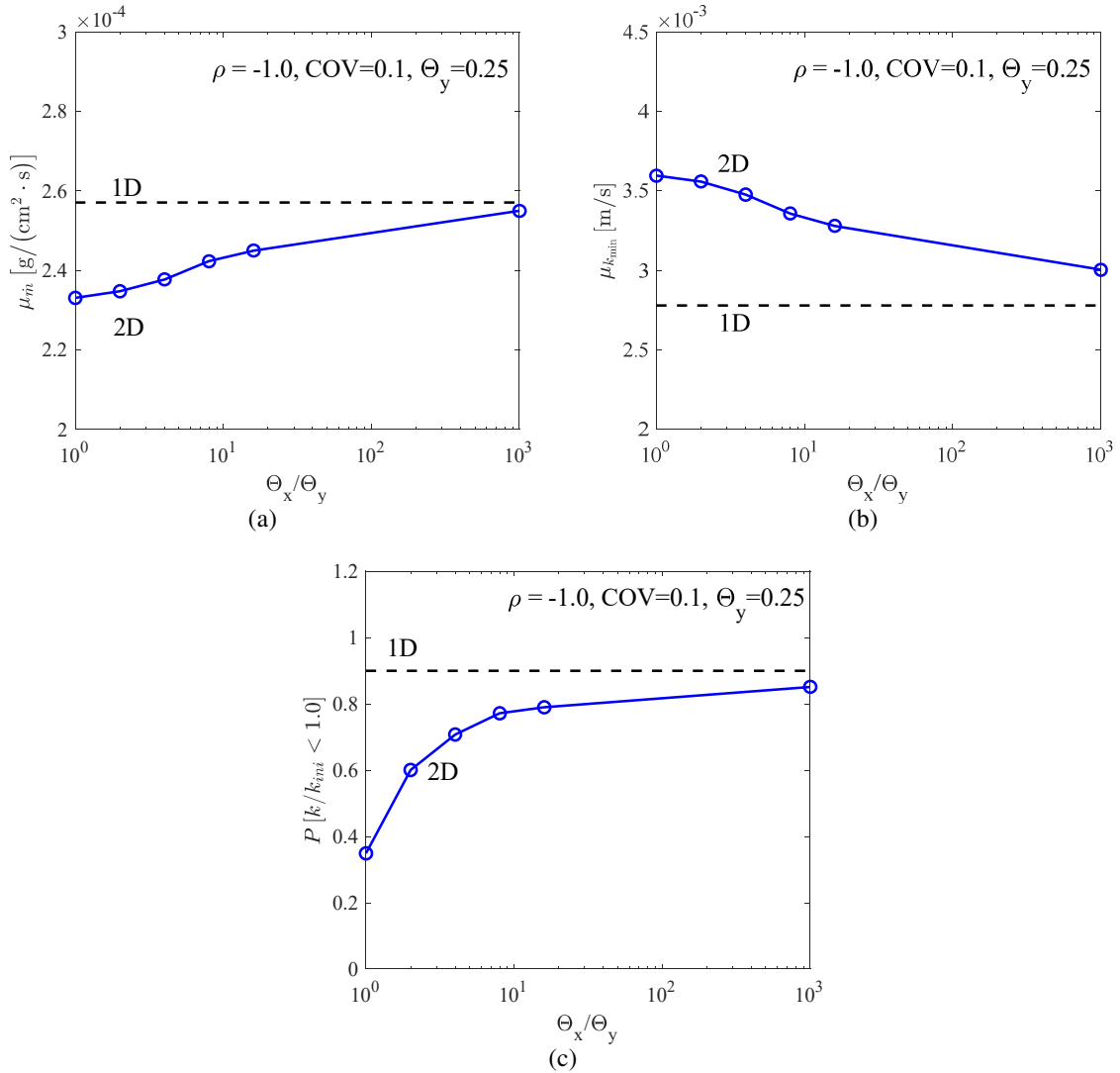


Figure 19. Comparison between 1D and 2D anisotropic analyses (a) mean of rate of eroded mass μ_m , (b) mean of minimum hydraulic conductivity during the test period $\mu_{k_{min}}$ and (c) probability of blockage

6 Conclusion and perspective

In this study, the influence of the soil heterogeneity on suffusion has been discussed by considering the initial porosity ϕ_0 and the fines content fraction f_{c0} as random fields. A four-

constituent model was implemented into a finite difference code together with a random field theory. Monte Carlo simulations of suffusion were conducted to investigate the influence of the variability, the spatial correlation length, and the cross correlation of ϕ_0 and f_{c0} on the rate of eroded mass and the minimum hydraulic conductivity during the test period. The most significant findings drawn from the results of this study are summarized as follows.

First, a four-constituent continuum finite difference model for suffusion has been extended throughout the self-filtration process. The model is therefore able to describe the temporal behavior with regard to both eroded soil and permeability change as observed in laboratory experiments. The deterministic simulations clearly show that the assumption of soil homogeneity is insufficient in predicting for instance the decrease of the hydraulic conductivity.

Secondly, in 1D Monte Carlo analyses, an increase of the variability in ϕ_0 and f_{c0} , or a decrease of the spatial correlation length of the variables generally decreases the mean rate of the eroded mass and the mean minimum hydraulic conductivity. Greater variability leads to more significant changes of soil porosity at the interface of different layers; the lower spatial correlation lengths cause the layers to become more uneven, producing more interfaces between loose and dense layers, both of them in turn facilitate the capture of the fine particles transported by the water flow. The susceptibility of soil to internal erosion based on the evaluation of the rate of erosion may be different to that obtained in a deterministic analysis of a homogeneous soil. Furthermore, even if the sample behavior is more strongly affected by the soil variability and spatial correlation, and somewhat less so by the cross-correlation between ϕ_0 and f_{c0} , negatively correlated ϕ_0 and f_{c0} are more likely to cause blockage leading to the potential increase of excess pore pressure and, thus, a strength degradation.

The results of 2D analyses confirm that the influx can bypass the local blockage. The mean rates of the eroded mass in 2D condition are generally smaller than in 1D condition. Interestingly, the greatest probability of blockage in 2D isotropic random fields occurs when the spatial correlation length is about half of the specimen length.

It should be noted that these conclusions have been formulated on the basis of results obtained under a simple geometry in 1D and 2D conditions. This study should be helpful for extending the approach to more complex geometries and boundary conditions in 2D and 3D conditions. In the future, an enhanced constitutive model considering the influence of the porosity and the fines content on the soil behavior will be implemented to account for the hydro-mechanical coupling of suffusion problems.

Acknowledgement

The financial supports provided by the National Natural Science Foundation of China (51579179) and the National Institute for Industrial Environment and Risks of France (INERIS) are gratefully acknowledged.

Appendix A. Finite difference solution for 2D internal erosion process

The system of partially differential equations can be solved in 2D conditions by:

$$\frac{\phi_{i,j}^{k+1} - \phi_{i,j}^k}{\Delta t} + [A_\phi]_i^k \frac{\phi_{i,j}^{k+1} - \phi_{i-1,j}^{k+1}}{\Delta z} + [A_\phi]_j^k \frac{\phi_{i,j}^{k+1} - \phi_{i,j-1}^{k+1}}{\Delta x} + [B_\phi]_{i,j}^k \phi_{i,j}^{k+1} + [C_\phi]_{i,j}^k = 0 \quad \dots\dots\dots(1)$$

with

$$[A_\phi]_i^k = \frac{u_{xi,j}^{k+1} - u_{xi,j}^k}{\Delta t}, [A_\phi]_j^k = \frac{u_{zi,j}^{k+1} - u_{zi,j}^k}{\Delta t}, [B_\phi]_{i,j}^k = -\frac{\epsilon_{vi,j}^{k+1} - \epsilon_{vi,j}^k}{\Delta t}, [C_\phi]_{i,j}^k = \frac{\epsilon_{vi,j}^{k+1} - \epsilon_{vi,j}^k}{\Delta t} + [\hat{n}]_{i,j}^k$$

$$\frac{c_{i,j}^{k+1} - c_{i,j}^k}{\Delta t} + [A_c]_i^k \frac{c_{i,j}^{k+1} - c_{i-1,j}^{k+1}}{\Delta z} + [A_c]_j^k \frac{c_{i,j}^{k+1} - c_{i,j-1}^{k+1}}{\Delta x} + [B_c]_{i,j}^k c_{i,j}^{k+1} + [C_c]_{i,j}^k = 0 \quad \dots\dots\dots(2)$$

$$\text{with } [A_c]_i^k = \left(\left[\frac{q_{w,x}}{\phi} \right]_{i,j}^k + \frac{u_{xi,j}^{k+1} - u_{xi,j}^k}{\Delta t} \right), [A_c]_j^k = \left(\left[\frac{q_{w,y}}{\phi} \right]_{i,j}^k + \frac{u_{yi,j}^{k+1} - u_{yi,j}^k}{\Delta t} \right),$$

$$[B_c]_{i,j}^k = \frac{1}{\phi_{i,j}^k} \left(\frac{\phi_{i,j}^{k+1} - \phi_{i,j}^k}{\Delta t} + [\text{div}(\mathbf{q}_w)]_{i,j}^k + \frac{\phi_{i,j+1}^k - \phi_{i,j-1}^k}{2\Delta x} \frac{u_{xi,j}^{k+1} - u_{xi,j}^k}{\Delta t} + \frac{\phi_{i+1,j}^k - \phi_{i-1,j}^k}{2\Delta z} \frac{u_{zi,j}^{k+1} - u_{zi,j}^k}{\Delta t} - \phi_{i,j}^k \frac{\epsilon_{vi,j}^{k+1} - \epsilon_{vi,j}^k}{\Delta t} \right),$$

$$[C_c]_{i,j}^k = [\hat{n}/\phi]_{i,j}^k$$

$$\frac{p_{wi,j}^{k+1} - p_{wi,j}^k}{\Delta t} - \frac{[A_{p_w}]_{i+1/2}^k (p_{wi+1,j}^{k+1} - p_{wi,j}^{k+1}) + [A_{p_w}]_{i-1/2}^k (p_{wi,j}^{k+1} - p_{wi-1,j}^{k+1})}{(\Delta z)^2} \dots\dots\dots(3)$$

$$- \frac{[A_{p_w}]_{j+1/2}^k (p_{wi,j+1}^{k+1} - p_{wi,j}^{k+1}) + [A_{p_w}]_{j-1/2}^k (p_{wi,j}^{k+1} - p_{wi,j-1}^{k+1})}{(\Delta x)^2} = 0$$

with

$$[A_{p_w}]_{i-1/2}^k = \left(\frac{0.5}{[A_{p_w}]_{i-1,j}^k} + \frac{0.5}{[A_{p_w}]_{i,j}^k} \right)^{-1}, \quad [A_{p_w}]_{i+1/2}^k = \left(\frac{0.5}{[A_{p_w}]_{i,j}^k} + \frac{0.5}{[A_{p_w}]_{i+1,j}^k} \right)^{-1},$$

$$[A_{p_w}]_{j-1/2}^k = \left(\frac{0.5}{[A_{p_w}]_{i,j-1}^k} + \frac{0.5}{[A_{p_w}]_{i,j}^k} \right)^{-1}, \quad [A_{p_w}]_{j+1/2}^k = \left(\frac{0.5}{[A_{p_w}]_{i,j}^k} + \frac{0.5}{[A_{p_w}]_{i,j+1}^k} \right)^{-1},$$

$$[A_{p_w}]_{i,j}^k = \left[\frac{K_{\text{MOD}} k(f_c, \phi)}{\eta \bar{\rho}(c)} \right]_{i,j}^k$$

where with $\mathbf{u}(u_x, u_z)$ indicating the displacement field of the soil skeleton. The volumetric strain ε_v are then calculated under small strain assumption using an elastic model with bulk modulus K_{MOD} .

References

- [1] Foster M, Fell R, Spannagle M. The statistics of embankment dam failures and accidents. *Canadian Geotechnical Journal*. 2000;37(5):1000-24.
- [2] Fell R, Fry J-J. The state of the art of assessing the likelihood of internal erosion of embankment dams, water retaining structures and their foundations. *Internal Erosion of Dams and their Foundations*, Robin Fell & Jean-Jacques Fry—editors, Taylor & Francis. 2007.
- [3] Fry J-J, Vogel A, Royet P, Courivaud J-R. Dam failures by erosion: lessons from ERINOH data bases. *ICSE6 Paris*. 2012:273-80.
- [4] Shen S-L, Xu Y-S. Numerical evaluation of land subsidence induced by groundwater pumping in Shanghai. *Canadian Geotechnical Journal*. 2011;48(9):1378-92.
- [5] Shen S, Wang Z, Cheng W. Estimation of lateral displacement induced by jet grouting in clayey soils. *Geotechnique*. 2017;67(7):621-30.
- [6] Wu H-N, Shen S-L, Yang J. Identification of tunnel settlement caused by land subsidence in soft deposit of Shanghai. *Journal of Performance of Constructed Facilities*. 2017;31(6):04017092.
- [7] Fell R, Wan CF, Cyganiewicz J, Foster M. Time for development of internal erosion and piping in embankment dams. *Journal of geotechnical and geoenvironmental engineering*. 2003;129(4):307-14.
- [8] Wan CF, Fell R. Investigation of rate of erosion of soils in embankment dams. *Journal of geotechnical and geoenvironmental engineering*. 2004;130(4):373-80.
- [9] Bonelli S, Marot D. On the modelling of internal soil erosion. *The 12th International Conference of International Association for Computer Methods and Advances in Geomechanics (IACMAG)2008*. p. 7.
- [10] Fry J. Lessons on internal erosion in embankment dams from failures and physical models. *Scour and Erosion: Proceedings of the 8th International Conference on Scour and Erosion (Oxford, UK, 12-15 September 2016)*: CRC Press, 2016. p. 41.
- [11] Gombert P, Orsat J, Mathon D, Alboresha R, Al Heib M, Deck O. Role des effondrements karstiques sur les desordres survenus sur les digues de Loire dans le Val D'Orleans (France). *Bulletin of Engineering Geology and the Environment*. 2015;74(1):125-40.
- [12] Zhang L, Chen Q. Seepage failure mechanism of the Gouhou rockfill dam during reservoir water infiltration. *Soils and Foundations*. 2006;46(5):557-68.
- [13] Xu Y, Zhang L. Breaching parameters for earth and rockfill dams. *Journal of Geotechnical and Geoenvironmental Engineering*. 2009;135(12):1957-70.
- [14] Sterpi D. Effects of the erosion and transport of fine particles due to seepage flow. *international journal of Geomechanics*. 2003;3(1):111-22.
- [15] Yin Z-Y, Huang H-W, Hicher P-Y. Elastoplastic modeling of sand–silt mixtures. *Soils and Foundations*. 2016;56(3):520-32.
- [16] Hu W, Hicher P-Y, Scaringi G, Xu Q, Van Asch T, Wang G. Seismic precursor to instability induced by internal erosion in loose granular slopes. *Géotechnique*. 2018:1-13.
- [17] Skempton A, Brogan J. Experiments on piping in sandy gravels. *Geotechnique*. 1994;44(3):449-60.
- [18] Reddi LN, Lee I-M, Bonala MV. Comparison of internal and surface erosion using flow pump tests on a sand-kaolinite mixture. *Geotechnical Testing Journal*. 2000;23(1):116-22.

- [19] Bendahmane F, Marot D, Rosquoët F, Alexis A. Characterization of internal erosion in sand kaolin soils: Experimental study. *Revue européenne de génie civil*. 2006;10(4):505-20.
- [20] Bendahmane F, Marot D, Alexis A. Experimental parametric study of suffusion and backward erosion. *Journal of Geotechnical and Geoenvironmental Engineering*. 2008;134(1):57-67.
- [21] Moffat R, Fannin RJ, Garner SJ. Spatial and temporal progression of internal erosion in cohesionless soil. *Canadian Geotechnical Journal*. 2011;48(3):399-412.
- [22] Chang D, Zhang L. A stress-controlled erosion apparatus for studying internal erosion in soils. *Geotechnical Testing Journal*. 2011;34(6):579-89.
- [23] Marot D, Rochim A, Nguyen H-H, Bendahmane F, Sibille L. Assessing the susceptibility of gap-graded soils to internal erosion: proposition of a new experimental methodology. *Natural Hazards*. 2016;83(1):365-88.
- [24] Rochim A, Marot D, Sibille L, Thao Le V. Effects of Hydraulic Loading History on Suffusion Susceptibility of Cohesionless Soils. *Journal of Geotechnical and Geoenvironmental Engineering*. 2017;143(7):04017025.
- [25] Sherard JL, Dunnigan LP, Talbot JR. Filters for silts and clays. *Journal of Geotechnical Engineering*. 1984;110(6):701-18.
- [26] Kenney T, Chahal R, Chiu E, Ofoegbu G, Omenge G, Ume C. Controlling constriction sizes of granular filters. *Canadian Geotechnical Journal*. 1985;22(1):32-43.
- [27] Ke L, Takahashi A. Experimental investigations on suffusion characteristics and its mechanical consequences on saturated cohesionless soil. *Soils and Foundations*. 2014;54(4):713-30.
- [28] Aboul Hosn R. Suffusion and its effects on the mechanical behavior of granular soils: numerical and experimental investigations: Grenoble Alpes, 2017.
- [29] Ke L, Takahashi A. Triaxial erosion test for evaluation of mechanical consequences of internal erosion. *Geotechnical Testing Journal*. 2014;37(2):347-64.
- [30] Vanmarcke EH. Probabilistic modeling of soil profiles. *Journal of the geotechnical engineering division*. 1977;103(11):1227-46.
- [31] DeGroot DJ, Baecher GB. Estimating autocovariance of in-situ soil properties. *Journal of Geotechnical Engineering*. 1993;119(1):147-66.
- [32] Dasaka S, Zhang L. Spatial variability of in situ weathered soil. *Géotechnique*. 2012;62(5):375.
- [33] Freeze RA. Probabilistic one-dimensional consolidation. *Journal of Geotechnical and Geoenvironmental Engineering*. 1977;103(ASCE 13067).
- [34] Badaoui Mh, Nour A, Slimani A, Berrah MK. Consolidation statistics investigation via thin layer method analysis. *Transport in porous media*. 2007;67(1):69-91.
- [35] Huang J, Griffiths DV, Fenton GA. Probabilistic analysis of coupled soil consolidation. *Journal of Geotechnical and Geoenvironmental Engineering*. 2009;136(3):417-30.
- [36] Griffiths DV, Fenton GA. Probabilistic slope stability analysis by finite elements. *Journal of Geotechnical and Geoenvironmental Engineering*. 2004;130(5):507-18.
- [37] Griffiths DV, Huang J, Fenton GA. Probabilistic infinite slope analysis. *Computers and Geotechnics*. 2011;38(4):577-84.
- [38] Fenton GA, Griffiths DV. Bearing-capacity prediction of spatially random $c \ \phi$ soils. *Canadian geotechnical journal*. 2003;40(1):54-65.

- [39] WANG Y. Reliability-based design of spread foundations by Monte Carlo simulations. *Géotechnique*. 2011;61(8):677-85.
- [40] Schaufler A, Becker C, Steeb H. Infiltration processes in cohesionless soils. *ZAMM - Journal of Applied Mathematics and Mechanics/Zeitschrift für Angewandte Mathematik und Mechanik*. 2013;93(2 - 3):138-46.
- [41] Revil A, Cathles L. Permeability of shaly sands. *Water Resources Research*. 1999;35(3):651-62.
- [42] Uzuoka R, Ichiyama T, Mori T, Kazama M. Hydro-mechanical analysis of internal erosion with mass exchange between solid and water. 6th International Conference on Scour and Erosion 2012. p. 655-62.
- [43] Cividini A, Bonomi S, Vignati GC, Gioda G. Seepage-induced erosion in granular soil and consequent settlements. *International Journal of Geomechanics*. 2009;9(4):187-94.
- [44] Zhong C. Study of Soil Behavior Subjected to An Internal Erosion Process Université de Nantes, 2018.
- [45] Guide MUs. The mathworks. Inc, Natick, MA. 1998;5(333).
- [46] Fenton GA, Vanmarcke EH. Simulation of random fields via local average subdivision. *Journal of Engineering Mechanics*. 1990;116(8):1733-49.
- [47] Fenton GA. Error evaluation of three random-field generators. *Journal of Engineering Mechanics*. 1994;120(12):2478-97.
- [48] Jin YF, Yin ZY, Shen SL, Hicher PY. Selection of sand models and identification of parameters using an enhanced genetic algorithm. *International Journal for Numerical and Analytical Methods in Geomechanics*. 2016;40(8):1219-40.
- [49] Yin ZY, Jin YF, Shen JS, Hicher PY. Optimization techniques for identifying soil parameters in geotechnical engineering: Comparative study and enhancement. *International Journal for Numerical and Analytical Methods in Geomechanics*. 2018;42(1):70-94.
- [50] Suri A. Cleanup of internal filter cake during flowback 2005.
- [51] Al-Abduwani FAH. Internal filtration and external filter cake build-up in sandstones: TU Delft, Delft University of Technology, 2005.